frontiers | Frontiers in Materials

TYPE Original Research
PUBLISHED 04 August 2022
DOI 10.3389/fmats.2022.973829

OPEN ACCESS

EDITED BY
Yanjin Lu,
Fujian Institute of Research on the Structure of Matter (CAS), China

REVIEWED BY
Liang-Yu Chen,
Jiangsu University of Science and Technology, China
Yi Yang,
University of Shanghai for Science and Technology, China
Chao Chen,
Central South University, China

*CORRESPONDENCE
Shujun Li,
shjli@imr.ac.cn
Yue Zhu,
zhuyuedr@163.com

SPECIALTY SECTION
This article was submitted to Biomaterials, a section of the journal Frontiers in Materials

RECEIVED 20 June 2022
ACCEPTED 08 July 2022
PUBLISHED 04 August 2022

CITATION
Yuan W, Zhao X, Li S and Zhu Y (2022), Effect of laser scanning speed on microstructure and mechanical properties of SLM porous Ti-5Al-5V-5Mo-3Cr-1Fe alloy.
Front. Mater. 9:973829.
doi: 10.3389/fmats.2022.973829

Effect of laser scanning speed on microstructure and mechanical properties of SLM porous Ti-5Al-5V-5Mo-3Cr-1Fe alloy

Wei Yuan[1], Xiaoli Zhao[2], Shujun Li[3]* and Yue Zhu[1]*

[1]Department of Orthopedics, The First Hospital of China Medical University, Shenyang, China, [2]Institute of Materials Science, School of Materials Science and Engineering, Northeastern University, Shenyang, China, [3]Shi-changxu Innovation Center for Advanced Materials, Institute of Metal Research, Chinese Academy of Sciences, Shenyang, China

In this study, porous Ti-55531(Fe) was fabricated by selective laser melting (SLM) with different laser scanning speeds. The microstructures, surface morphology, inner defects, porosity, microhardness, and compressive behaviors were studied. The variation of lattice constant and hardness were analyzed. The results show that all the specimens have a density of ~1 g/cm^3, and a Vicker's hardness with a range of 280–320 Hv0.1. The porosity of the SLM-produced materials is greater than the designed value (77%) and increases from 77.33% to 82.33% with the increase of laser scanning speed from 500 mm/s to 1,500 mm/s. Continuous irregular columnar dendrites, a large number of gas-induced defects with small size between 20 and 60 μm and a deep molten pool form in the specimens fabricated with a laser scanning speed less than 1,000 mm/s. Some defects, elongated voids and interrupted columnar dendrites are identified in the specimens fabricated with the laser scanning speed more than 1,000 mm/s caused by the insufficient input energy. All specimens with different laser scanning speeds show the single ß phase patterns. The compressive strength of the specimens with the laser scanning speed of 500 mm/s is maintained at 32 MPa and the compressive strength decreases with the increase of laser scanning speed. The specimens with a scanning speed of 500 mm/s present the best mechanical properties and surface quality.

KEYWORDS

metamaterial, beta-titanium, microstructure, mechanical behavior, selective laser melting

Introduction

Recently, 3D-architected metamaterials with micro-lattice structures have shown considerable weight reduction efficiency, flexible design capability and especially potential applications in battery electrodes, shock energy damping, acoustic, biological implants, and thermal sensors or stretchable electronics (Barba et al., 2020; Yu et al., 2020; Zhang et al., 2020; Kelly et al., 2021a; Kelly et al., 2021b; Salmi, 2021; Timercan et al., 2021; du Plessis et al., 2022). Meanwhile, additive manufacturing (AM) is widely accepted as a new

forming process for high performance components in aerospace, medical, energy and automotive applications due to its unique features of rapid prototyping, complex or customized processing and high efficiency (Chen et al., 2021). Various micro truss lattice structures can be achieved by AM method without limit of configuration of cell and the complexity of the structural surface. Selective laser melting (SLM) emerging as an advanced manufacturing technologies to fuse powders track-by-track and grow layer-by-layer under the control of a CAD model, is capable of fabricating porous 3D-architectures with optimal properties for various applications. Developing metallic lattice structures (e.g., aluminum alloys, titanium alloys, and superalloys) with high strength and good ductility has become the mainstream of additive manufacturing.

Based on the chemical compositions and relative amounts of the α phase with hexagonal close-packed (hcp) structure and β phase with body-centered cubic (bcc) structure at room temperature, titanium alloys are typically classified as α alloy, near-α alloy, $\alpha + \beta$ alloy, near-β alloy, and β alloy. Due to the superior strength, cold workability, corrosion resistance and biocompatibility, β alloys have attracted lots of attentions in aerospace, marine and biomedical industry (Chen et al., 2020; Zhang and Chen, 2020; Liu et al., 2021). Beta titanium alloy Ti-5553 (Ti-5Al-5V-5Mo-3Cr-0.5Fe) alloy is known as a heat treatable beta titanium alloy for its high strength and good ductility and has been widely applied as large aerospace components such as landing gears, arresting hooks and flap tracks (Huang et al., 2011; Ghosh et al., 2013; Cotton et al., 2015; Qin et al., 2016). The mechanical performance can be further improved by increasing the iron content from 0.5 wt% to 1 wt% (Guan et al., 2008). The strength and elongation of Ti-55531 (Fe) (Ti-5Al-5V-5Mo-3Cr-1Fe) alloy can be maintained at 1,350 MPa and 15.5%, respectively after STA heat treatment (Guan et al., 2008). To date, there have been some basic studies of dense SLM Ti-5553 components on the machinability (Grove et al., 2018) and the evolution of microstructure and tensile properties after isothermal heat treatments (Carton et al., 2019). The strength and the ductility of SLM dense Ti-5553 are approximately as 1,088 MPa and 14%, respectively after heat treatment (Carton et al., 2019), which is comparable to those of SLM Ti64 (Ti-6Al-4V) product (Simonelli et al., 2014). For Ti64, the mechanical properties are sensitive to the cooling rates. Further factors such as process parameters, build geometry, scanning strategy and surrounding conditions affecting the thermal history and cooling rates will determine the microstructure and resulted properties (Chen et al., 2021). Therefore, there could be similar changes in SLM porous Ti-55531(Fe), which may contribute to the high strength and ductility of porous metallic materials (Yuan et al., 2018; Ren et al., 2019; Liu et al., 2020; Chen et al., 2021). However, to the best of our knowledge, there are few reports on the fabrication and mechanical properties of SLM porous Ti55531(Fe) in the literature.

In this study, porous Ti-55531(Fe) specimens were fabricated by SLM process with different laser scanning speeds. The effects of scanning speed on the microstructure, surface morphology, porosity and compressive behaviors were investigated.

TABLE 1 Chemical composition of Ti-55531(Fe) powders used for SLM process (wt%).

	Al	V	Cr	Mo	Fe	Ti
Ti-55531(Fe)	5.11	5.53	2.87	3.56	1.13	Balanced

Materials and methods

The chemical compositions of the gas atomization (GA) Ti-55531(Fe) pre-alloyed powder are shown in Table 1. The Ti-55531 powders show a regular spherical morphology and a size distribution with a range of 20–70 μm and an average particle size (d_{50}) of 45 μm (Figure 1). The surface morphology and chemical compositions of the GA powders and the as-SLMed specimens were analyzed by SEM (JSM-6510A) assembled with an energy dispersive spectrometer (EDS). And a laser scattering particle size distribution analyzer (Horiba, LA-920) was used to determine the powder size distribution.

A 10 mm^3 × 10 mm^3 × 10 mm^3 3D scaffold architecture cube arrayed by rhombic dodecahedron unit cells was generated using Magic software (Materialise, Belgium) and built in an SLM system (Realizer SLM 100 machine with a 200 W Yb: YAG fiber laser). The schematic diagram for SLM process of rhombic dodecahedron designed 3D lattice structure is shown in Figure 2. The laser power was 190 W, the diameter of the focused spot was 20 μm, the thickness of the fixed powder layer and scanning interval was 30 and 60 μm, and the scanning rate were between 500 and 1,500 mm/s. The phase constitution of the lattice samples was determined by Rigaku Smartlab X-ray diffraction (XRD). Metallography was performed to determine microstructural changes of porous structures with different laser scanning speeds. These samples were prepared by grinding to 3,000 mesh, mirror polishing with SiO_2 suspension and followed by etching in acid mixture (HF: HNO_3: H_2O = 1:2:50). The shape of the molten pool is approximated by an arc in the building direction and the depth of the molten pool is reflected by the curvature radius of the approximate arc. The pool size could be changed along the building direction, so the average curvature radius of the fusion line was calculated by measuring more than fifteen fusion lines in the metallography figures.

The X-ray tomography (micro-CT) has been reported as computed tomography (CT) technology to check the surface roughness and of mesh struts and inner defects in the metallic cellular structures (Chan and Young, 2013; Wang et al., 2013). An XRT work was carried out using an Xradia Versa XRM-500 system (Carl Zeiss X-ray Microscopy Inc., Pleasanton, California, United States) with a spatial resolution of micron even dozens of nanometers to check the topological mesh and the size and count distribution of the defects inside the samples. Surface roughness

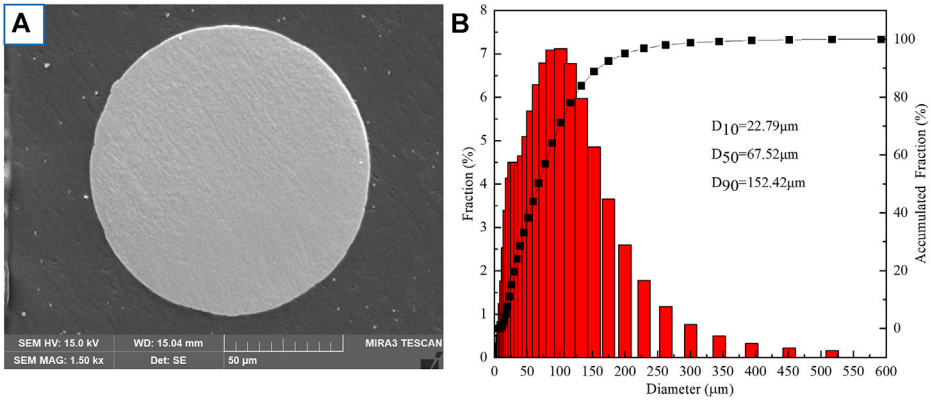

FIGURE 1
SEM micrographs of cross-section **(A)**, particle size distribution **(B)** of Ti55531 powders.

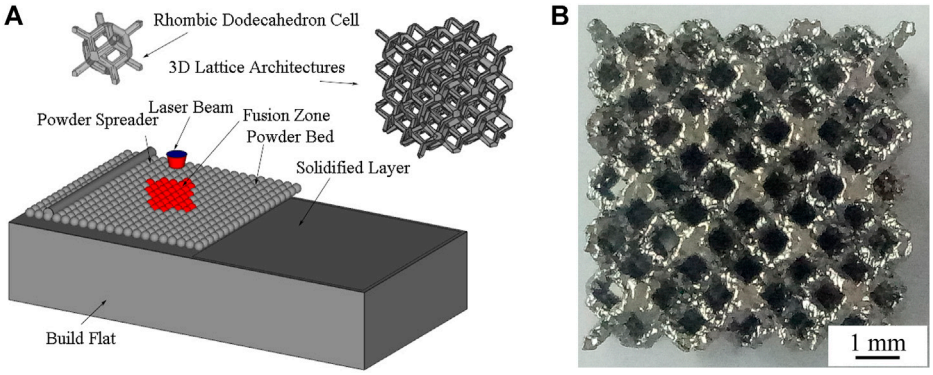

FIGURE 2
Schematic diagram of SLM process **(A)** and side view of mesh arrays part **(B)** for rhombic dodecahedron designed 3D lattice architecture.

is evaluated by analyzing the surface morphology based on the Micro-CT slicing data. The average roughness (R_a) is calculated as Eq. 1 (Chen et al., 2021)

$$R_a = \frac{1}{N}\sum_{i=1}^{N}|f_n| \tag{1}$$

where f_n is the length of the protruding at N locations on the surface of the struts based on the Micro-CT slicing data.

The porosity can be calculated by Eq. 2.

$$P = \frac{V_0 - V}{V_0} \times 100\% = 1 - \frac{D}{D_t} \tag{2}$$

where the V_0 is the total volume of the material, V is the volume of solid material, D is the measured density and the D_t is the theoretical density. The theoretical density (D_t) of Ti-55531(Fe) is presented as Eq. 3.

$$D_t = \sum_{1}^{n} d_i \cdot \eta_i \tag{3}$$

where D_t is the theoretical density, d_i is the atomic density of the ith atom and η_i is the atomic percentage of the ith atom in Ti-55531(Fe) alloys. The measured density of the SLM Ti-55531(Fe) was determined by the modified Archimedes method using a direct reading electronic hydrometer (ET-320), as is shown in Eq. 4 (Liu et al., 2016b)

$$D = \frac{W_1 \cdot D_0}{W_3 - W_2}. \tag{4}$$

where D_0 is the density of the water, W_1 is the weight of porous specimens in air, W_2 is the weight of porous specimens in water after water osmosis stabilization and W_3 is the weight of porous specimens in air after water osmosis stabilization.

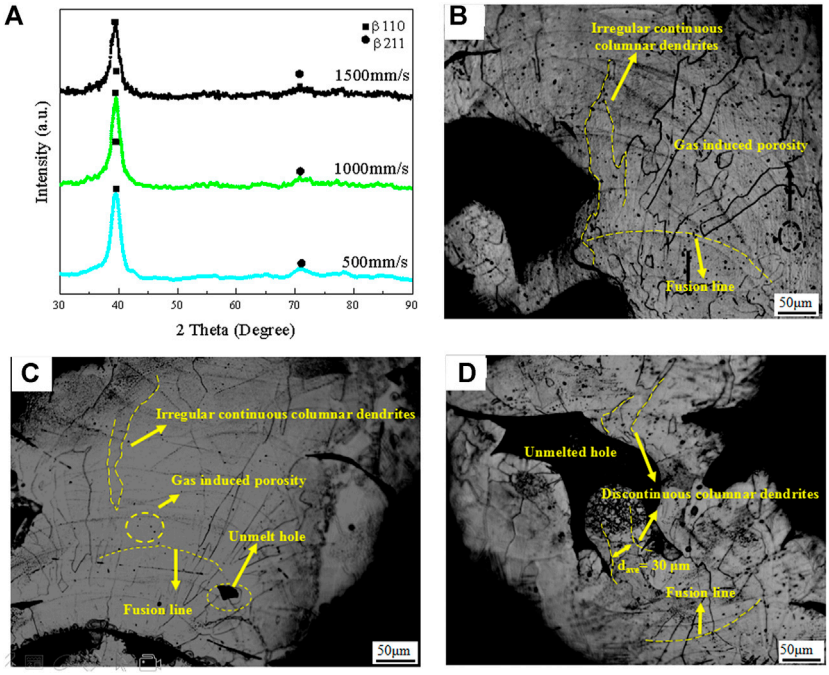

FIGURE 3
XRD profiles **(A)**, optical micrographs of materials built at 500 mm/s **(A)**, 1000 mm/s **(B)**, 1500 mm/s **(C)**.

Vicker's microhardness tests were conducted by 401 MVD™ with a 100 g load and a 10 s dwell time. The hardness was measured at the horizontal surface with the maximum number of the struts which is around 9 mm from the substrate depending on the different porous structure. Random measurement of five points was conducted on the surface of the cellular samples using a single point mode. The lattice constant was quantitatively calculated by Kohn least square method (Zhang et al., 2009) according to Eq. 4.

$$\sum_{j=1}^{M}\sum_{i=1}^{N} C_{ji}C_{li}X_j = \sum_{i=1}^{N}\frac{1}{d_i^{\exp 2}}C_{li}\,(l = 1, \cdots, M) \tag{5}$$

where N is the number of the crystal planes for calculation, and for b.c.c. structure $M = 1$, $X_1 = 1/a^2$, $C_1 = h^2+k^2+l^2$, $d_i^{\exp}$ is the experimental value of the crystal plane spacing. And the variance of X_1 can be calculated according Eq. 5.

$$\sigma^2(X_{ii}) = \frac{2\chi^2 A_{ii}^{-1}}{N - M} \tag{6}$$

A is a matrix with an element $a_{ij} = \sum_{i=1}^{N} C_{ij}C_{li}$, A_{ii}^{-1} is the ith diagonal element of the inverse matrix of matrix A, $\chi^2 = \frac{1}{2}\sum_{i=1}^{N}(\frac{1}{d_i^{\exp 2}} - \sum_{j=1}^{M} X_j C_{ji})$

Uniaxial compression tests were carried out by a uniaxial testing machine (Shimazu AG-X plus, 100 KN) with a speed of 0.5 mm/min at ambient temperature. The loading direction was parallel to the building direction. The specimens were continually loaded and all the tests were stopped near 3 kN. Specific strength was calculated based on compressive strength and the measured density.

Results and discussion

Microstructure

As is shown in Figure 3A, the single β phase peaks are identified in as-built SLM Ti-55531 (Fe) alloy. This is different from the α (hcp) and β phases found in EBM Ti-24Sn-4Zr-8Sn component reported by Liu et al. (2016a) and the complicated structure in NiTiNb alloy prepared by eutectic reaction reported by Wang et al. (2018). As the cooling rate in SLM process is very high, the microstructure (β phase) at high temperature can be retained at ambient temperature. The laser scanning speed has limited effect on the phase type of the Ti55531 (Fe) alloys. When the laser scanning speed is less than 1,000 mm/s, the joints of the samples consist of irregular continuous columnar dendrites along the building direction, and fusion lines with small average radius of curvature (923–1,003 μm) are obvious (Figures 3B,C). Discontinuous columnar dendrites can be identified in the sample fabricated with a laser scanning speed of 1,500 mm/s, and fusion line is hard to be found due to a larger

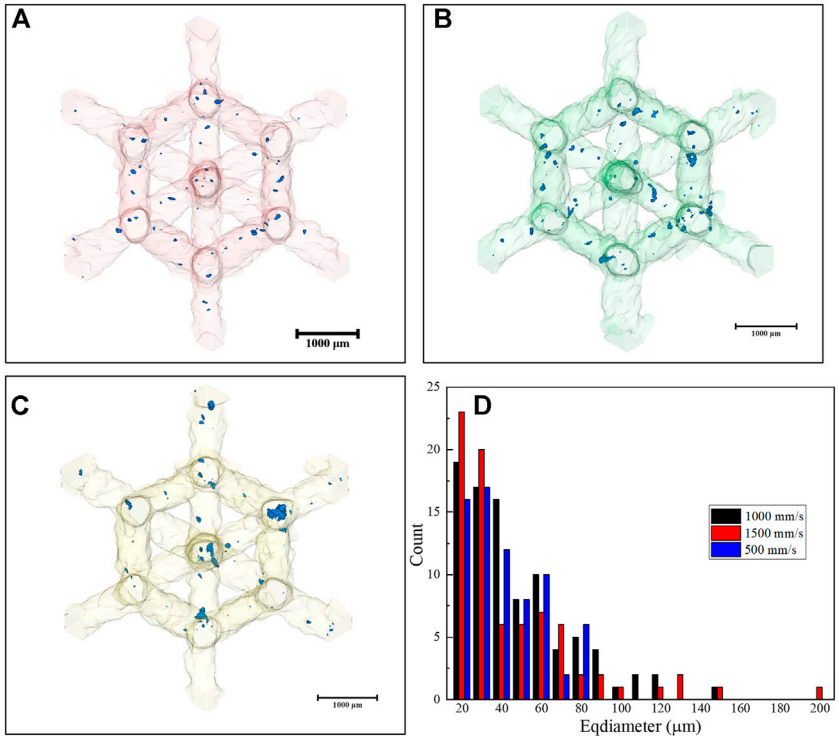

FIGURE 4
Morphology of the inner defects in the materials built at 500 mm/s **(A)**, 1000 mm/s **(B)**, 1500 mm/s **(C)**, and size and distribution of the inner defects in the materials fabricated with different laser scanning speeds **(D)**.

average radius of curvature (~1,095 μm) (Figure 3D). The irregular columnar dendrites along the thermal flow direction can be ascribed to the cyclic heat treatment response during the layer-by-layer SLM process.

The porosity of porous materials is determined by the open holes (apparent porosity), surface morphology (surface roughness) and inner defects.

There is an energy volume density (E_v) to investigate the porosity, it is calculated as (Chen et al., 2021):

$$E_v = \frac{P}{v \cdot t_1 \cdot h_s} \tag{7}$$

where v is laser scanning speed, t_l is layer thickness and h_s is hatch spacing. The laser scanning speed is inversely proportional to the input energy. Input energy density decrease with the increase of the laser scanning speed.

Inner defects

The morphologies of the inner defects in the samples built at 500 mm/s, 1000 mm/s, 1500 mm/s are shown in Figures 4A–C, respectively. The size and number of the defects inside the samples built at different laser scanning speeds are shown in Figure 4D. Lower scanning speed (500 mm/s) leads to a large number of inner defects with a small size in the range of 20–80 μm (Figures 4A,D). Small size defects is still visible, but medium size defects (90–150 μm) appears when the scanning speed increases from 500 mm/s to 1,000 mm/s (Figures 4B,D). Inner defects with average size larger than 150 μm form and the number of small size inner defects decreases when the scanning speed increases from 1,000 mm/s to 1,500 mm/s (Figures 4C,D).

Homogenous porous structures always own advantages over both of the relative density of porous structure and the mechanical strength (Zhang and Wang, 2018). Besides the change of the microstructure and surface roughness on the mesh struts with different laser scanning speed, the size and count distribution of defects inside the basic cell may be responsible for the mechanical performance. The inner defects with small particle size distribution (20–60 μm) are mainly induced by the element volatilization in keyhole mode (Chen et al., 2021), are distributed in all samples built at different scanning speeds. But the number of the small size defects decreases slightly and the inner defects with large size increase by an increase of laser scanning speed. This phenomenon is because the input energy density at higher scanning speed is

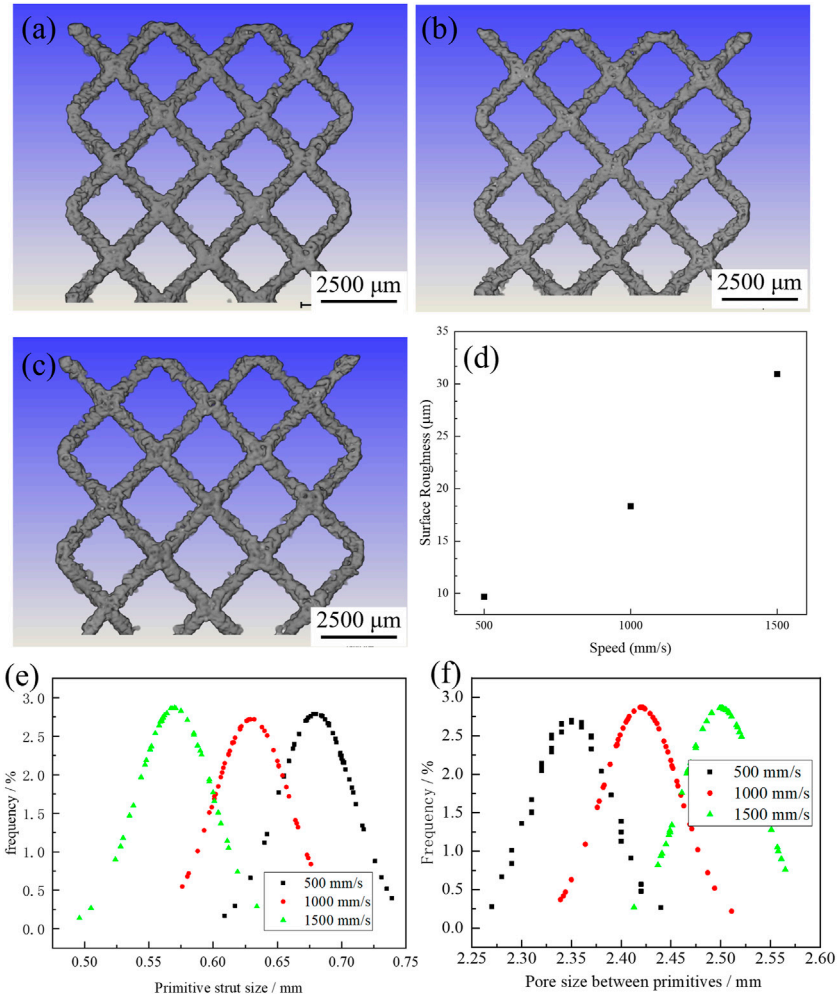

FIGURE 5
Micro-CT surface morphologies of the materials built at 500 mm/s **(A)**, 1,000 mm/s **(B)**, 1,500 mm/s **(C)**. Surface roughness **(D)**, strut size **(E)**, and pore size **(F)** of porous structures built at different laser scanning speeds.

insufficient to maintain the keyhole mode, and insufficient depth of molten pool enhances the susceptibility of the lack of fusion zone.

Surface morphology

The surface morphology of the materials built at different laser scanning speeds is shown in Figures 5A–C. The surface roughness, pore size, and the strut size of the mesh arrays are analyzed according to the Micro-CT surface morphology and shown in Figures 5D–F, respectively. The surface of the material built at 500 mm/s is the smoothest (R_a = 10 μm) (Figure 5A,D) with the largest strut of 0.62 mm and the smallest pore of 2.35 mm. The surface roughness increases from 10 to 31 μm with the laser scanning speed increased to 1,500 mm/s. And the strut size decreases from 620 to 570 μm and hole size increases from 2.35 to 2.50 mm, accordingly. Sample fabricated with a scanning speed of 500 mm/s has a structure with an average hole size of 2.35 mm and an average strut size of 680 μm. The strut size decreases to 630 μm and hole size increase to 2.42 mm in the sample fabricated with a scanning speed of 1,000 mm/s. And the strut size continues to decrease to 570 μm and hole size continue to increase to 2.50 mm in the sample fabricated with a scanning speed of 1,500 mm/s. The porous material consists primarily of struts and holes. Larger holes and smaller struts mean more unfilled space in the porous sample and higher apparent porosity. As shown in Figure 6, the scanning speed also has effect on the actual strut size, with increasing the scanning speed from 500 mm/s to 1,500 mm/s, the strut size change from 0.48–0.63 mm to 0.61–0.74 mm, which is larger than the designed value of 0.48 mm.

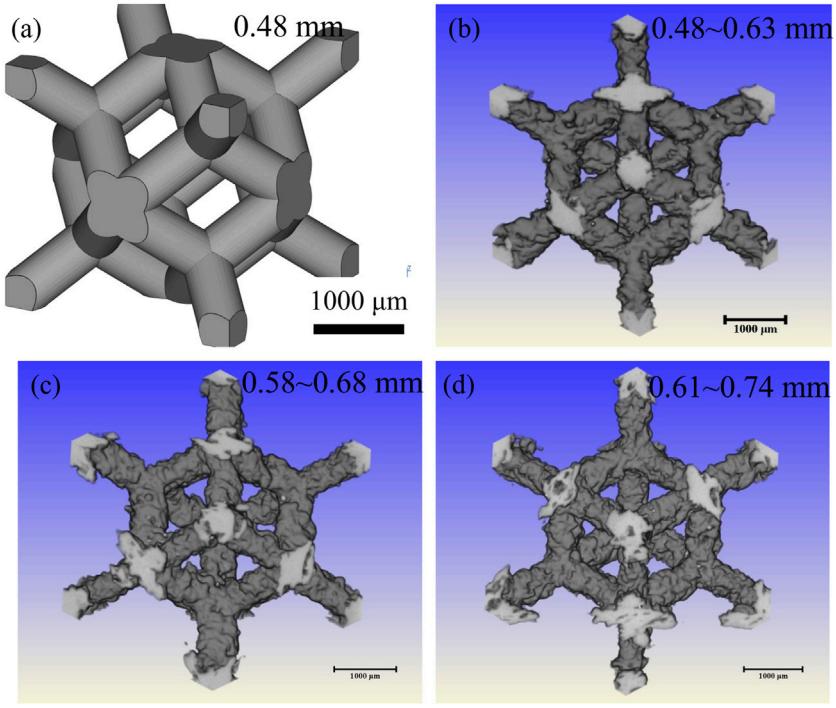

FIGURE 6
The size of the designed rhombic dodecahedral scaffold **(A)**, compare it with the actual size of the strut fabricated using different scanning speeds of 500 mm/s **(B)**, 1,000 mm/s **(C)** and 1,500 mm/s **(D)**.

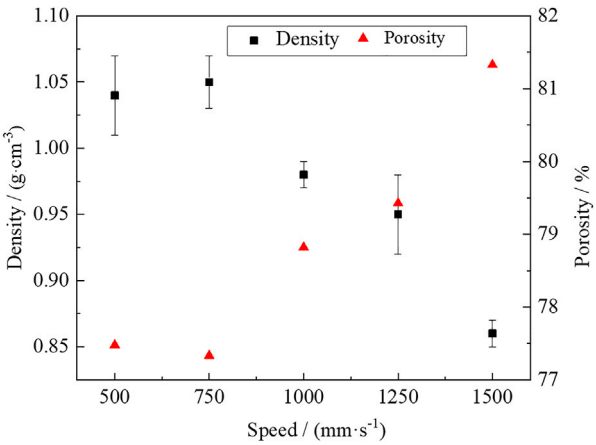

FIGURE 7
Densities and porosity of the SLMed-porous materials as a function of laser scanning speed.

Surface roughness is one of the important indicators of both of the porous and dense components prepared in SLM process and can ultimately affect the part performance. When a high laser scanning speed is used, the energy input is insufficient to fully melt the metallic powders (Chen et al., 2021). Some of the powders remain in the surface of the porous structure. Small balls form in the molten pool due to the plateau Raleigh capillary instability and move to the edge of the molten pool with the surface tension of molten pool. The surface roughness increases by an increase of the scanning speed because of an insufficient melting of metallic powders in total.

Porosity

The density and porosity of the SLM porous samples built at different scanning speed are shown in Figure 7. The densities of the samples decrease from 1.05 g/cm^3 to 0.85 g/cm^3 with the increase of laser scanning speed. The measured porosity is a little higher than the designed porosity (77%) and increase from 77.33% to 82.33% with the increase of laser scanning speed from 500 mm/s to 1,500 mm/s.

A high input energy density at a low scanning speed leads to a deep molten pool with a small average radius of curvature of 923 μm. Deep molten pool can promote the full melting of the metallic powders and reduce the defects of large size on the surface. The molten pool is elongated and can be broken into small islands at high scanning speed due

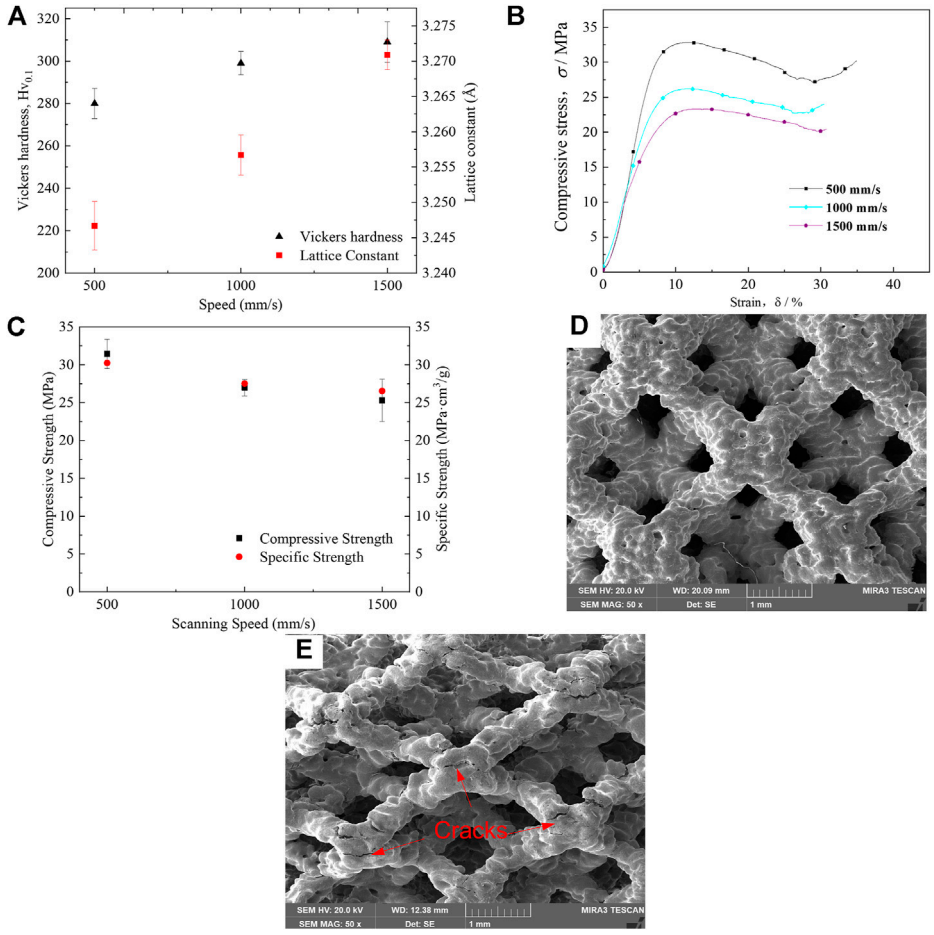

FIGURE 8
Lattice constant and microhardness **(A)**, the compressive stress-strain curves of the materials with different scanning speeds **(B)**, compressive strength and specific strength for SLM porous Ti-55531(Fe) alloys with different laser scanning speeds **(C)**, SEM micrographs of materials with scanning speed of 1,000 mm/s in pre-compression **(D)** and post-compression state **(E)**, respectively.

to the plateau Raleigh capillary instability (Chen et al., 2021). Inadequate penetration of molten pool will cause the lack of fusion defects. The shallower molten pool leads to unmelted holes and even discontinuous columnar dendrites.

In higher energy volume density, deep molten pool promotes element volatilization, and the volatilization gas can induce porosity. In this study, gas induced porosities with small size are dominated and both of the apparent porosity and the surface roughness are the lowest in the samples built at a scanning speed of 500 mm/s. Rapid scanning reduces the pool depth and enhances the stability of elongated lack of fusion defects and even interrupted the continuous growth of the columnar grains due to the plateau Raleigh capillary instability. Elongated voids with sharp edge form in the final parts and can be a resource of stress concentration under applied loads.

Microhardness and compressive behavior

The microhardness ($Hv_{0.1}$) and the lattice constant increase with increasing scanning speed (Figure 8A). The factors affecting microhardness may include the phase constitution, the surface roughness and the surface residual thermal stress. All the samples show the same phase constitution as mentioned in Figure 3A. In this study, the residual thermal stress is evaluated by the lattice distortion based on the XRD data. The lattice distortion is mainly related to the vacancy concentration (Hu et al., 2010). The vacancies concentration can be lowered by decreasing the molten pool temperature. A higher scanning speed can lead to a shallower molten pool with a lower temperature because of a lower input energy density. The energy required to form Schottky vacancies is much less than that of Frenkel vacancies (Hu et al., 2010). Therefore, the atoms leaving the equilibrium position

mainly form Schottky defects, which results in the decrease of lattice constant. The lattice constant decreases with increasing vacancy concentration. Thus, the lattice distortion decreases by increasing the laser scanning speed. Larger Schottky-mode lattice distortion enhances the tensile residual thermal stress on the surface of the samples. Residual thermal tensile stress on the surface reduces the resistance of the indenter head of the hardness tester to enter the material surface, thus showing low hardness.

Figure 8B shows the compressive stress-strain curves of materials prepared with different scanning speed. It can be seen that they exhibit the similar curve shape but different strength. Figure 8C shows the compressive strength and specific strength of samples built at different laser scanning speed. The compressive strength can reach 31 MPa in the sample fabricated with a laser scanning speed of 500 mm/s and decreases with the increase of the laser scanning speed. The compressive strength decreases to 25 MPa in the samples built at 1,500 mm/s. The highest specific strength of as-built SLM porous Ti-55531 (Fe) specimens is 30.2 MPa cm^3/g at the scanning speed of 500 mm/s and decreases with the increase of the laser scanning speed. The specific strength decrease to 26.5 MPa cm^3/g when the scanning speed increase to 1,500 mm/s.

Porosity is the dominant factor on the compressive stress (Kadirgama et al., 2018). In this study, porosity increase with the increase of laser scanning speed, and high porosity can induce low compressive strength. High porosity is mainly related to large size unfused defects and small size of strut size. Firstly, rapid scanning speed reduced the size of the molten pool, and insufficient penetration of molten pool led to large size unfused defects. Large size unfused defects can be resources of the stress concentration under applied loads and reduce the compressive strength. Secondly, an increase of the scanning speed can decrease the size of the mesh strut which reducing the bearing capacity of the porous sample.

After compression, some structural units of the sample are deformed along the loading direction in two-dimensional: the hole spacing along the loading direction decreases, and the hole spacing perpendicular to the loading direction increases. All the samples fabricated with different laser scanning speeds show breakdown in cell nodes perpendicular to the direction of loading after the compression (Figures 8D,E), indicating that the strength of 3D rhombic dodecahedron cell designed porous structure is significantly depending on the design of the unit structure.

Conclusion

In this work, different laser scanning speed was used to fabricate a β type Ti-55531(Fe) meta-material with a 3D rhombic dodecahedron cell designed porous structure. The effects of scanning speed on microstructural change, porosity, and compressive behaviors were systematically studied and discussed. The results are summarized as follows:1) The columnar grains are continuous and deep molten pool forms with the laser scanning speed of 500 mm/s. The melt pool becomes shallower with increasing the scanning speed from 500 mm/s to 1,500 mm/s. The continuous growth of β columnar grains can be interrupted due to plateau Raleigh capillary instability or inadequate melting when the laser speed is 1,500 mm/s. 2) Experimental porosities (77.33–82.33%) are higher than expected (77%). The surface roughness (10–30 μm) of porous SLMed Ti-55531(Fe) alloys is at the range level of particle size distribution. The inner defects with a size of 20–60 μm are distributed all over the samples built at different scanning speed. And the number of tiny inner defects with a range of 20–80 μm decreases and large inner defects with a range of 120–200 μm form by an increase of scanning speed. 3) All the specimens show a range of 280–310 for Hv0.1 and 25–31 MPa for compressive strength. The specific strength of samples with scanning speed less than 1,000 mm/s is in a range of 27.5–30.2 MPa cm^3/g and the roughness is less than 20 μm. The specific strength is 26.5 MPa cm^3/g and the surface roughness increase to near 30 μm when the scanning speed increase to 1,500 mm/s. Scanning speed of 500 mm/s is good for both of the mechanical properties and surface quality.

Data availability statement

The original contributions presented in the study are included in the article/supplementary material, further inquiries can be directed to the corresponding authors.

Author contributions

WY and XZ: Concept, data curation, investigation, writing-original draft. SL and YZ: Conceptualization, writing-original draft, formal analysis, review and editing.

Funding

This work was supported partially by Chinese MoST (2017YFC1104903), Key Research Program of Frontier Sciences, CAS (QYZDJ-SSW-JSC031-02), National Natural Science Foundation of China (81902191, 51871220, 51922026), Scientific Research Foundation of Educational Department of Liaoning Province (QN2019001), China Postdoctoral Science Foundation (2021M693523), State Key Laboratory of Light Alloy Casting Technology for High-end Equipment (LACT-007), Shenyang Talents program

(RC200230) and CAS Interdisciplinary Innovation Team Project (JCTD-2020-10).

Conflict of interest

The authors declare that the research was conducted in the absence of any commercial or financial relationships that could be construed as a potential conflict of interest.

Publisher's note

All claims expressed in this article are solely those of the authors and do not necessarily represent those of their affiliated organizations, or those of the publisher, the editors and the reviewers. Any product that may be evaluated in this article, or claim that may be made by its manufacturer, is not guaranteed or endorsed by the publisher.

References

Barba, D., Alabort, C., Tang, Y. T., Viscasillas, M. J., Reed, R. C., Alabort, E., et al. (2020). On the size and orientation effect in additive manufactured Ti-6Al-4V. *Mat. Des.* 186, 108235. doi:10.1016/j.matdes.2019.108235

Carton, H. D., Klein, K. D., and Elmer, J. W. (2019). Evolution of microstructure and mechanical properties of selective laser melted Ti-5Al-5V-5Mo-3Cr after heat treatments. *Sci. Technol. Weld. Join.* 24, 465–473. doi:10.1080/13621718.2019.1594589

Chan, Y. S., and Young, I. K. (2013). Void ratio and durability properties of porous polymer concrete using recycled aggregate with binder contents for permeability pavement. *J. Appl. Polym. Sci.* 126, E338–E348. doi:10.1002/app.36974

Chen, L. Y., Cui, Y. W., and Zhang, L. C. (2020). Recent development in beta titanium alloys for biomedical applications. *Metals* 10 (9), 1139. doi:10.3390/met10091139

Chen, L. Y., Liang, S. X., Liu, Y., and Zhang, L. C. (2021). Additive manufacturing of metallic lattice structures: Unconstrained design, accurate fabrication, fascinated performances and challenges. *Mater. Sci. Eng. R Rep.* 146, 100648. doi:10.1016/j.mser.2021.100648

Cotton, J. D., Briggs, R. D., Boyer, R. R., Tamirisakandala, S., Russo, P., Shchetnikov, N., et al. (2015). State of the art in beta titanium alloys for airframe applications. *JOM* 67, 1281–1303. doi:10.1007/s11837-015-1442-4

du Plessis, A., Razavi, S. M. J., Benedetti, M., Murchio, S., Leary, M., Watson, M., et al. (2022). Properties and applications of additively manufactured metallic cellular materials: A review. *Prog. Mat. Sci.* 125, 100918. doi:10.1016/j.pmatsci.2021.100918

Ghosh, A., Sivaprasad, S., Bhattacharjee, A., and Kar, S. K. (2013). Microstructure-fracture toughness correlation in an aircraft structural component alloy Ti-5Al-5V-5Mo-3Cr. *Mater. Sci. Eng. A* 568, 61–67. doi:10.1016/j.msea.2013.01.017

Grove, T., Denkena, B., Maiss, O., Krodel, A., Schwab, H., Kuhn, U., et al. (2018). Cutting mechanism and surface integrity in milling of Ti-5553 processed by selective laser melting. *J. Mech. Sci. Technol.* 32, 4883–4892. doi:10.1007/s12206-018-0936-8

Guan, J., Liu, Y. Y., and Lei, J. F. (2008). *The influences of heat-treatment and alloying on the microstructures and mechanical properties of Ti-5Al-5Mo-5V based alloys*. Beijing: Master, Graduate School of the Chinese Academy of Science.

Hu, G. X., Cai, X., and Rong, Y. H. (2010). *Fundamentals of materials science*. Shanghai: Shanghai Jiaotong University Press.

Huang, J., Wang, Z. R., and Xue, K. M. (2011). Cyclic deformation response and micromechanisms of Ti alloy Ti-5Al-5V-5Mo-3Cr-0.5Fe. *Mater. Sci. Eng. A* 528, 8723–8732. doi:10.1016/j.msea.2011.08.045

Kadirgama, K., Harun, W. S. W., Tarlochan, F., Samykano, M., Ramasamy, D., Azir, M. Z., et al. (2018). Statistical and optimize of lattice structures with selective laser melting (SLM) of Ti6AL4V material. *Int. J. Adv. Manuf. Technol.* 97 (1-4), 495–510. doi:10.1007/s00170-018-1913-1

Kelly, C. N., Kahra, C., Maier, H. J., and Gall, K. (2021a). Processing, structure, and properties of additively manufactured titanium scaffolds with gyroid-sheet architecture. *Addit. Manuf.* 41, 101916. doi:10.1016/j.addma.2021.101916

Kelly, C. N., Wang, T., Crowley, J., Wills, D., Pelletier, M. H., Westrick, E. R., et al. (2021b). High-strength, porous additively manufactured implants with optimized mechanical osseointegration. *Biomaterials* 279, 121206. doi:10.1016/j.biomaterials.2021.121206

Liu, Y. J., Li, S. J., Hou, W. T., Wang, S. G., Hao, Y. L., Yang, R., et al. (2016a). Electron beam melted beta-type Ti-24Nb-4Zr-8Sn porous structures with high strength-to-modulus ratio. *J. Mat. Sci. Technol.* 32 (6), 505–508. doi:10.1016/j.jmst.2016.03.020

Liu, Y. J., Li, S. J., Wang, H. L., Hou, W. T., Hao, Y. L., Yang, R., et al. (2016b). Microstructure, defects and mechanical behavior of beta-type titanium porous structures manufactured by electron beam melting and selective laser melting. *Acta Mat.* 113, 56–67. doi:10.1016/j.actamat.2016.04.029

Liu, Y. J., Ren, D. C., Li, S. J., Wang, H., Zhang, L. C., Sercombe, T. B., et al. (2020). Enhanced fatigue characteristics of a topology-optimized porous titanium structure produced by selective laser melting. *Addit. Manuf.* 32, 101060. doi:10.1016/j.addma.2020.101060

Liu, Z. Y., He, B., Lyu, T. Y., and Zou, Y. (2021). A review on additive manufacturing of titanium alloys for aerospace applications: Directed energy deposition and beyond Ti-6Al-4V. *JOM* 73 (6), 1804–1818. doi:10.1007/s11837-021-04670-6

Qin, D. Y., Li, Y. L., Zhang, S. Y., and Zhou, L. (2016). On the tensile embrittlement of lamellar Ti-5Al-5V-5Mo-3Cr alloy. *J. Alloys Compd.* 663, 581–593. doi:10.1016/j.jallcom.2015.12.158

Ren, D. C., Li, S. J., Wang, H., Hou, W. T., Hao, Y. L., Jin, W., et al. (2019). Fatigue behavior of Ti-6Al-4V cellular structures fabricated by additive manufacturing technique. *J. Mat. Sci. Technol.* 35, 285–294. doi:10.1016/j.jmst.2018.09.066

Salmi, M. (2021). Additive manufacturing processes in medical applications. *Materials* 14 (1), 191. doi:10.3390/ma14010191

Simonelli, M., Tse, Y. Y., and Tuck, C. (2014). Effect of the build orientation on the mechanical properties and fracture modes of SLM Ti-6Al-4V. *Mater. Sci. Eng. A* 616, 1–11. doi:10.1016/j.msea.2014.07.086

Timercan, A., Sheremetyev, V., and Brailovski, V. (2021). Mechanical properties and fluid permeability of gyroid and diamond lattice structures for intervertebral devices: Functional requirements and comparative analysis. *Sci. Technol. Adv. Mat.* 22, 285–300. doi:10.1080/14686996.2021.1907222

Wang, L. Q., Xie, L. C., Zhang, L. C., Chen, L. Y., Ding, Z. H., Lv, Y. T., et al. (2018). Microstructure evolution and superelasticity of layer-like NiTiNb porous metal prepared by eutectic reaction. *Acta Mat.* 143, 214–226. doi:10.1016/j.actamat.2017.10.021

Wang, S. G., Wang, S. C., and Zhang, L. (2013). Application of high resolution transmission X-ray tomography in material science. *Acta Metall. Sin.* 49 (8), 897. doi:10.3724/sp.j.1037.2013.00107

Yu, G. S., Li, Z. B., Li, S. J., Zhang, Q., Hua, Y., Liu, H., et al. (2020). The select of internal architecture for porous Ti alloy scaffold: A compromise between mechanical properties and permeability. *Mat. Des.* 192, 108754. doi:10.1016/j.matdes.2020.108754

Yuan, W., Hou, W. T., Li, S. J., Hao, Y. L., Yang, R., Zhang, L. C., et al. (2018). Heat treatment enhancing the compressive fatigue properties of open-cellular Ti-6Al-4V alloy prototypes fabricated by electron beam melting. *J. Mat. Sci. Technol.* 34, 1127–1131. doi:10.1016/j.jmst.2017.12.003

Zhang, L. C., and Chen, L. Y. (2020). A review on biomedical titanium alloys: recent progress and prospect. *Adv. Eng. Mat.* 21 (4), 1801215. doi:10.1002/adem.201801215

Zhang, L., and Wang, S. G. (2018). Correlation of materials property and performance with internal structures evolvement revealed by laboratory X-ray tomography. *Materials* 11 (10), 1795. doi:10.3390/ma11101795

Zhang, M. K., Yang, Y. Q., Qin, W. T., Wu, S. B., Chen, J., Song, C. H., et al. (2020). Optimizing the pinch-off problem for gradient triply periodic minimal surface cellular structures manufactured by selective laser melting. *Rapid Prototyp. J.* 26, 1771–1781. doi:10.1108/rpj-11-2019-0298

Zhang, Q. L., Wang, Y. S., Xiao, J., Li, D. Q., and Yin, S. T. (2009). Lattice distortion by the least square method. *Chin. J. Quantum. Elec.* 26, 177–186. doi:10.3969/j.issn.1007-5461.2009.02.010